AGU100 ADVANCING EARTH AND SPACE SCIENCE

Geophysical Research Letters

RESEARCH LETTER
10.1029/2019GL083955

# Controls on Eolian Landscape Evolution in Fractured Bedrock

**Jonathan P. Perkins**[1], **Noah J. Finnegan**[2], **Shanaka L. de Silva**[3], **and Michael J. Willis**[4]

[1]Geology, Minerals, Energy, and Geophysics Science Center, U.S. Geological Survey, Menlo Park, CA, USA, [2]Department of Earth and Planetary Sciences, University of California, Santa Cruz, CA, USA, [3]College of Earth, Oceanic, and Atmospheric Science, Oregon State University, Corvallis, OR, USA, [4]Cooperative Institute for Research in Environmental Sciences, University of Colorado Boulder, Boulder, CO, USA

**Key Points:**
- In wind-eroded bedrock landscapes, particle abrasion can focus along fracture networks or cross-cut them, yielding unique landform patterns
- These erosion patterns emerge from a competition between flow strength, particle inertia, and topographic steering by fractured bedrock
- Understanding aerodynamic and structural thresholds can help with interpretations of abrasion processes across planetary landscapes

**Supporting Information:**
- Supporting Information S1

**Correspondence to:**
J. P. Perkins,
jperkins@usgs.gov

**Citation:**
Perkins, J. P., Finnegan, N. J., de Silva, S. L., & Willis, M. J. (2019). Controls on eolian landscape evolution in fractured bedrock. *Geophysical Research Letters*, *46*, 12,012–12,020. https://doi.org/10.1029/2019GL083955

Received 31 MAY 2019
Accepted 6 OCT 2019
Accepted article online 17 OCT 2019
Published online 8 NOV 2019

**Abstract** Wind abrasion is important for planetary landscape evolution, and wind-abraded bedrock landscapes contain many landforms that are difficult to interpret. Here we exploit a natural experiment in Chile where topographic shielding by an upwind lava flow yields diverse erosional landforms in a downwind ignimbrite. Using a 3-D topographic wind model, we find that low velocities in the wake of a lava lobe coincide with a transition from landforms reflecting fracture-parallel erosion to flow-parallel erosion. Erosion rates across these landforms vary with shear velocity and abrasion susceptibility of the windward escarpment. We hypothesize that this morphologic threshold is controlled by whether particles can be lofted in suspension and overcome topographic steering imposed by fractured bedrock blocks. Within a phase space set by Rouse and Stokes numbers, our data illustrate that wind-abraded landforms reflect a competition between the material skeleton of the landscape and the strength of the flow that shapes it.

## 1. Introduction

Wind-abraded landscapes on Earth and Mars show evidence for erosion and sediment transport along fracture networks, as well as evidence for erosive features like yardangs and erosional furrows that can cross-cut the structural grain of landscapes (Bailey et al., 2007; Mandt et al., 2008) (supporting information Figure S1). In landscapes of fractured bedrock, these two wind-abrasional landforms may occur side by side, and although there has been significant work on wind abrasion mechanics in the past decades (e.g., Bridges & Laity, 2013; de Silva et al., 2013; Greeley et al., 1982; Hugenholtz et al., 2015; Pelletier, 2018; Pelletier et al., 2018; Perkins et al., 2015; Wang et al., 2011; Ward & Greeley, 1984), there is currently a lack of understanding what controls the emergence of diverse landscape-scale eolian erosion patterns and what can be inferred about geomorphic processes and past climate from their morphology. This is particularly true in volcanic bedrock where cooling joints can focus sediment transport and erosion, and where yardangs can form at multiple spatial scales (de Silva et al., 2010).

In this analysis we take advantage of a well-preserved ignimbrite surface that systematically transitions from a field of yardangs that cross-cut the internal cooling joint structure of the ignimbrite, to a network of erosional polygonal mesas isolated by fracture-controlled channels, and to a virtually uneroded ignimbrite surface, all in the lee of a young lava flow that serves to both modify the wind flow field and supply erosional tools (Figures 1 and S2). We simulate the influence of the upwind lava flow on the downwind velocity field across the ignimbrite surface using a 3-D topographic wind model and examine any linkages between topographically modulated surface shear velocity and landform shape. We also use satellite photogrammetry-derived high-resolution topographic data to characterize long-term erosion rates across the ignimbrite's distinct morphologic regimes. To examine controls on landscape evolution rates, we evaluate our results in the context of an eolian particle abrasion model. Lastly, we cast our calculated erosion rates and modeled shear velocity results within a dimensionless phase space that helps illustrate how feedbacks between flow strength, particle size, and obstacle geometry may lead to diverse erosional landforms.

## 2. Geomorphic Context and Observations

The Antofagasta region of Chile is a landscape replete with a diversity of wind-eroded landforms due to its arid climate and concentration of bedrock ignimbrites that are susceptible to wind erosion (Bailey et al.,

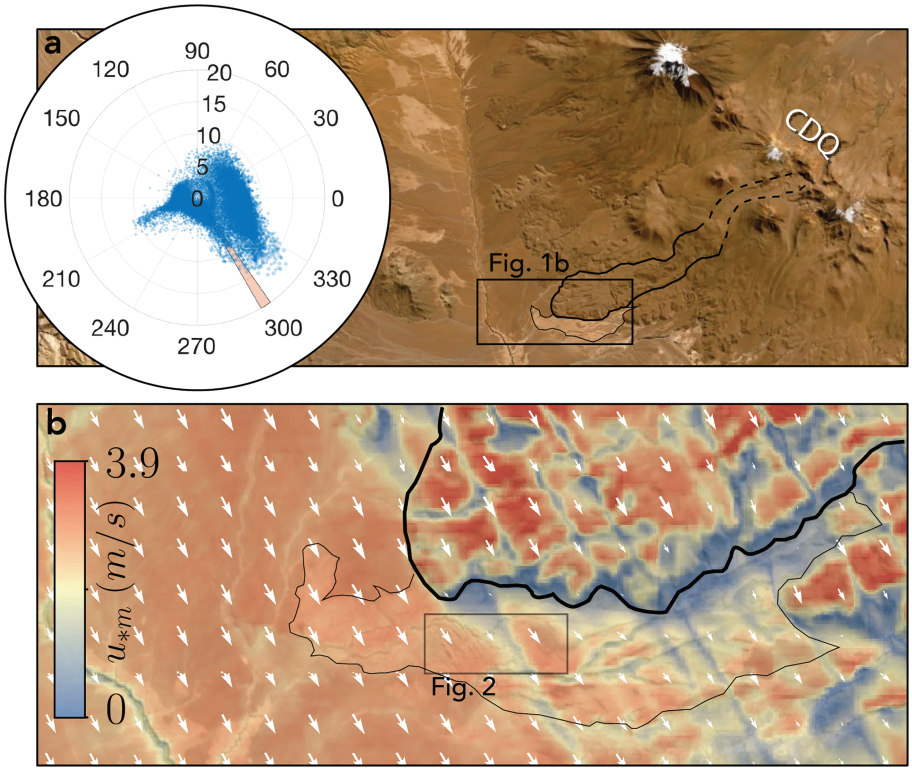


**Figure 1.** (a) Satellite imagery of the study area located along the western slope of the Central Andes, ~21 km SSW of Cerro Palpana in the Antofogasta region of Chile. UTM coordinates of top right and bottom left corners of the inset bounding box for Figure 1b are (540437 m E, 7588927 m S) and (536235 m E, 7595254 m S). Bold black line outlines a lava flow from Cerro de las Cuevas (CDQ) and is dashed where a moraine has overprinted the lava flow. Thin solid line demarcates the extent of the Carcote ignimbrite within the study area. Inset diagram is a scatter plot in arithmetic polar coordinates of regional hourly wind velocity measurements for the austral winter (June, July, and August), from NASA MERRA reanalysis data spanning 1981–2002. Blue dots reflect the magnitude and downwind direction the wind is blowing. Pink sector reflects the range in measured yardang orientations for the study area. (b) Zoom-in of study area showing 3-D topographic wind model results. Regional simulation was run with 30 m SRTM elevation data, and color scale corresponds to velocity magnitude for each 30 m grid cell. White vectors illustrate general wind directionality, and lengths are scaled by velocity. Thin and thick black lines outline the upwind lava flow and underlying ignimbrite, respectively.

2007; de Silva et al., 2010). Because of this, it is often utilized as a Martian analog landscape to understand eolian erosion processes within Martian formations like the Medussa Fossae formation, which displays a similar variety of wind erosion patterns to those observed on Earth (Mandt et al., 2008) and is also hypothesized to have an explosive volcanic origin (Ojha & Lewis, 2018).

Approximately 100 km north of the city of Calama along the Río Loa (Figure 1), the surface of the ~ 5.4 Ma Carcote ignimbrite (Baker & Francis, 1978) displays a systematic variation in erosion patterns from its eastern margin westward down toward the Río Loa valley axis (Figures S2 and 2a). The ignimbrite has a resistant caprock formed from vapor phase alteration by escaping gas in the cooling deposit, which is common for Central Andean ignimbrites (de Silva et al., 2010). Field observations of wind-eroded ignimbrites in Chile show that once the caprock is breached, headward wind erosion progresses predominantly by undermining of the weak lower tuff causing caprock blocks to topple (de Silva et al., 2010) and abrade in situ (Perkins et al., 2015).

The Carcote ignimbrite partially underlies an andesite flow originating from a volcanic dome upslope to the east in a chain of volcanic centers along the Incaliri lineament (de Silva & Francis, 1991). This chain progresses from the 3.6–3.8 Ma Cerro Palpana to the north (Worner et al., 2000) to Cerro del Azufre to the south (Figure 2b). The likely source of the lava flow is Cerro de las Cuevas, which has a K-Ar age of 3.15 ± 0.15 Ma (Worner et al., 2000).

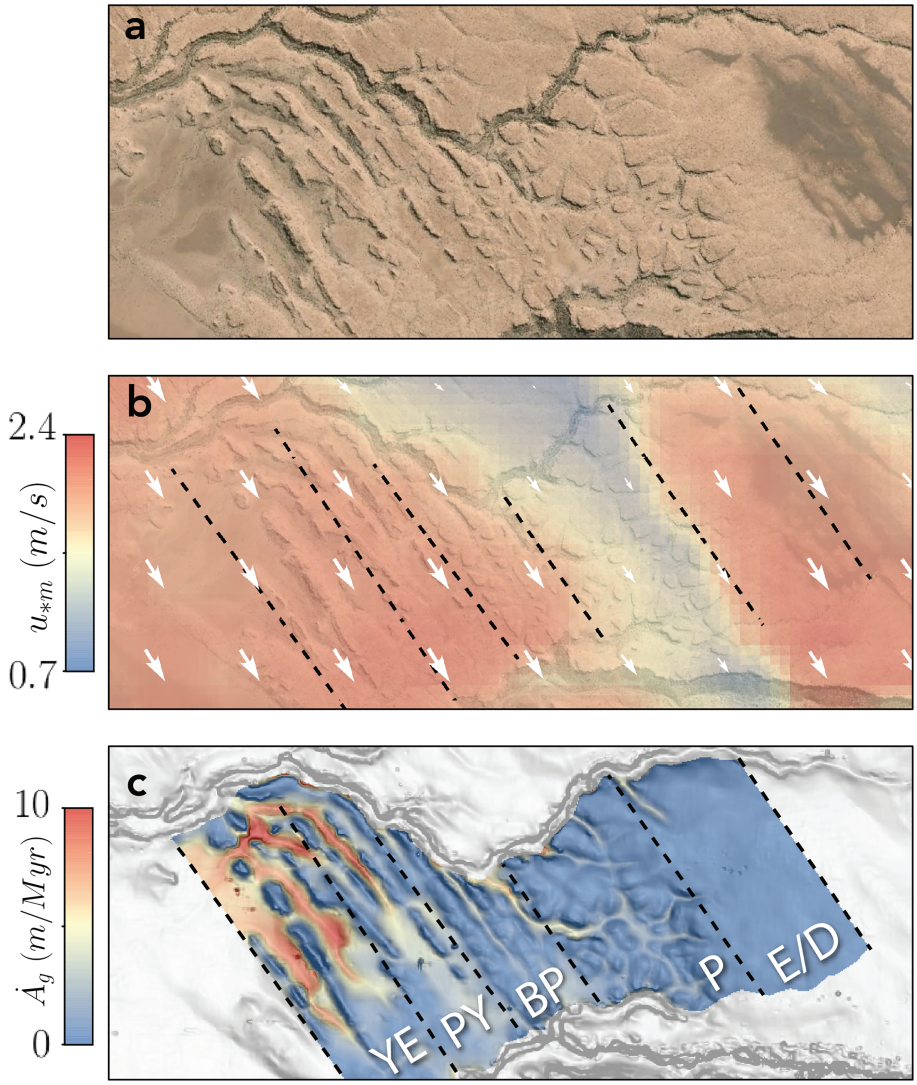


**Figure 2.** (a) Google Earth satellite imagery of zoom-in from Figure 1 (top left UTM coordinates: 540437 m E, 7588927 m S; bottom right coordinates: 536235 m E, 7595254 m S). Note deposition of sediment at eastern margin of study area. (b) Topographic wind model results overlain on satellite imagery for an input shear velocity of 2.0 m/s and an incident wind direction of 330°, parallel to yardang orientations. Zone of low velocity in the lee of the upwind andesite lobe tightly corresponds to zone of erosional polygons (see Figure 1b). Dashed lines demarcate zones described in c. (c) Map of geologic abrasion rates $A_g$ calculated from reconstructed ignimbrite surface using 3 m DEM. Slope map of DEM shown in grayscale. Dashed lines demarcate distinct erosion patterns from east to west in the downwind lee of the andesite flow. *YE* = yardangs and escarpment retreat; *PY* = polygon to yardang transition zone; *BP* = bisected polygons; *P* = eroded polygonal mesas; *E/D* = mixed erosion along fractures and upwind deposition (darker brown areas).

The ignimbrite surface slopes approximately due west, as evidenced by an incised tributary of the Río Loa at the northern margin of the exposed deposit (Figures S2 and 2a). This tributary drains off the overlying lava flow and appears to act as a structural seed for wind abrasion, both by creating a channel that can concentrate wind-transportable sediment and by providing a vertical escarpment that can be abraded by windblown particles (Figure 2a).

From the tight spatial coupling of the lava flow extent and the downwind erosion, and because sediment can be traced downwind from the andesite flow to the ignimbrite surface (Figures S2 and 2a), we infer that the lava flow emplacement initiated a phase of enhanced abrasion immediately downwind by supplying wind-transportable sediment. This is analogous to what has been observed in fluvial landscapes, like in the case of the 1999 Chi-chi earthquake in Taiwan where incision of an uplifted river reach was delayed for

~ 5 years until bedload transport of sediment resumed, resulting in 20 m of downcutting in 4 years (Cook et al., 2013). We can therefore estimate an age of abrasion initiating ranging from the ignimbrite depositional age of ~ 5.4 Ma to the lava flow age of 3.15 Ma. An additional complication is that, because the wind erosion initiates from the left bank of the channel, the channel must have existed before the onset of significant wind erosion. Therefore, the lava flow age is likely a maximum age for erosion initiation and erosion rates calculated using the lava flow age are likely minimum rates.

Across the Carcote ignimbrite we observe a systematic change in apparent erosion rates and patterns from east to west as the lava flow thins to its terminus (Figures 2 and S2). At the western edge of the study area (region *YE*, yardangs and escarpment retreat), a vertical escarpment is retreating as yardangs are carved in the remaining deposit. The yardangs are oriented NNW, consistent with yardang orientations spanning over 4° of latitude from 22°S to 26°S (e.g., de Silva et al., 2010) that reflect the influence of the subtropical westerly jet stream as it migrates to its northernmost maximum and flows over the high Central Andes during the austral winter and spring (e.g., Garreaud et al., 2003; Strecker et al., 2007; Vuille, 1999). As we discuss later, because wind abrasion rate is thought to be nonlinearly proportional to the wind shear velocity, the orientation of wind-abraded landforms should reflect strong and infrequent wind events (Anderson, 1986). Regional peak hourly wind velocities at 10 m elevation, as measured from NASA MERRA reanalysis data spanning 1981–2002, are also oriented in a NNW direction (blowing to the SSE) (Figure 1 inset). Although the data set is only decades long, the trends are consistent with a north-south turning of subtropical westerlies as they encounter land. Therefore, both the modern record and geologic proxy for intense wind directionality are consistent with forcing related to global circulation.

The entire depth of the ignimbrite deposit has been breached along region *YE*, exposing a relatively weak, slope-forming, brown, granular unit (Figure 2a). This change in lithology at the base of the windward escarpment is reflected in a higher magnitude of lateral erosion and deeper channelization (Figure 2c).

In the adjacent zone to the east (*PY*, polygon to yardang transition zone), escarpment retreat is less pronounced, and here yardangs are separated by linear erosional furrows that extend downwind off the edge of the ignimbrite at the next incised channel to the south, similar to what has been observed at the nearby Puripicar ignimbrite just east of the town of Calama (Perkins et al., 2015). Linear erosional troughs are a fundamental characteristic of yardang evolution and likely result from feedbacks between longitudinal turbulent flow structures in the atmospheric surface layer, sediment focusing, and subsequent erosion. These feedbacks were recently demonstrated through coupled numerical modeling (Pelletier, 2018). These furrows cross-cut the pattern of isotropic cooling joints (Figure 2a), again similar to what has been observed at the nearby Puripicar ignimbrite (Bailey et al., 2007; Perkins et al., 2015).

This cross-cutting of joint patterns is reflected well in the morphology at zone *BP* (bisected polygons), where erosion along cooling joints yields polygonal landforms about 15–20 m in diameter that are bisected by the linear NW/SE-trending furrows. Here the resultant erosional morphology appears to reflect a combination of sediment transport within fracture-controlled channels oblique to the primary wind direction, as well as within wind-parallel streaks.

Along region *P* (eroded polygonal mesas), wind-parallel erosional furrows are absent, and here erosional troughs are formed primarily along the cooling joints within the ignimbrite itself, yielding a network of isolated polygonal mesas ranging from ~ 0.5–3 m in height and approximately 30 m in diameter. This pattern resembles a small-scale, isotropic version of what has been deemed fretted terrain on Mars (Sharp, 1973), where isolated polygonal mesas hundreds of meters high are separated by what look like irregular fracture networks that often show evidence for eolian sediment transport parallel to fracture geometry (e.g., Mandt et al., 2008).

Lastly, in region $E/D$ (mixed erosion along fractures and upwind deposition), erosional landforms are largely absent along the windward escarpment, and deposition of sediment in the lee of small ridges and infilling of fractures can be seen in large patches (Figure 2a). The downstream edge of region $E/D$ marks the boundary where the channel incises through the uppermost caprock, above which channel relief is lower by 2–3 m on average (Figure S3). As we discuss later, it is likely that this variation in relative rock properties and channel relief prevents eolian abrasion and undercutting into the frontal escarpment (i.e., the channel's left-bank canyon sidewall).

These gradients in erosion rates and landscape morphology across the Carcote ignimbrite, in the lee of the overlying andesite flow, present a natural experiment that allows us to test whether regional scale aerodynamics control rates of wind-driven landscape evolution over million-year timescales. At a local scale, we can examine how varying flow strength relates to erosion pattern differences and better understand what thresholds arise that lead to flow-parallel or fracture-parallel abrasion.

## 3. Methods

We reconstruct the ignimbrite surface using a 3 m digital elevation model (DEM) that we created from Worldview satellite image photogrammetry using NASA Ames Stereo Pipeline software (Figure 2c). We first map bedrock polygon tops in ArcGIS and then create an interpolated surface projecting from the sheltered, uneroded ignimbrite zone. From the interpolated surface, we subtract the DEM elevations to get an estimate of vertical erosion for each grid cell (Figure 2b). Each subregion of the ignimbrite surface is designated by changes in mapped erosion patterns and from the satellite imagery in Google Earth (Figure 2c). For each designated process zone, we then calculate a bulk-average geologic abrasion rate $\dot{A}_g$ by dividing the total volume removed per map area since the erosion initiation time.

To model surface wind velocity, we use an open-source program called WindNinja, developed by the U.S. Forest Service Rocky Mountain Research Station Fire, Fuel, and Smoke Science Program. Originally developed for realistic tracking of fire over complex topography, the software uses a 3-D momentum-conserving solver based on the OpenFOAM computational fluid dynamics software and is therefore useful for examining the complex flow field in the lee of obstacles that may lead to flow separation and recirculation. Because of memory constraints, we use a 30 m SRTM DEM as the base topography. Although a DEM of this resolution successfully captures the large-scale effects of the upwind lava flow, it is too coarse to capture the higher-resolution flow field between individual polygonal structures.

To paramaterize our model, we use an incident wind direction parallel to the mean yardang orientation along the Carcote and an incident shear velocity of 2.0 m/s, equal to the peak gust shear velocities recorded from an airport weather station (SCCF) in Calama, Chile (Figure S4). Although the Calama airport is ~ 90 km SSW of our study area, regional wind patterns during the austral winter occur at the spatial scale of the subtropical jet stream and therefore span degrees of latitude (e.g., de Silva et al., 2010; Garreaud et al., 2003; Vuille, 1999). The resultant flow field pattern is sensitive to incident wind direction and relatively insensitive to incident flow velocity. For each mapped subregion, we calculate the average shear velocity of all the grid cells within the area.

## 4. Results and Discussion

### 4.1. Abrasion Rates

Geologic abrasion rates $\dot{A}_g$ along the Carcote ignimbrite range over 2 orders of magnitude, from 0.05 m/Myr at the easternmost zone $E/D$, where sediment deposition is visible, to 2.8 m/Myr at the westernmost zone *YE*, where the windward escarpment of the Carcote has actively retreated (Figure 3a). The largest reduction in erosion rates occurs between zones *YE* to zone *BP* and then tapers from the bisected polygons to the zone of mixed erosion and deposition $E/D$.

Figure 3a also includes a latitudinal profile from west to east of mean modeled shear velocities across each morphologic regime of the ignimbrite surface. $u_*$ values are slightly above the incident wind velocity for zones *YE* and *PY*, then begin to decline at *BP* as shear velocities decline in the low-velocity wake of the andesite lobe (Figures 1b and 2b). East of the wind shadow in zone *P*, shear velocities recover to mean flow conditions along zone $E/D$.

Long, linear zones of low velocity in the wake of topographic obstacles typically form from flow separation and the downwind stretching of vortices that occur at the margins of the obstacle. This phenomenon is commonly marked by the presence of high albedo streaks on Earth, Mars, and Venus (Greeley & Iversen, 1985) that reflect the preferential concentration of sediment toward the midline of the obstacle wake, and this process has been modeled in both wind tunnel simulations (Greeley et al., 1974) and numerical simulations (Burkow & Griebel, 2016). While the whole lava flow lee experiences low velocities, the relatively flat surface and three-dimensionality of the lobe at the terminus of the andesite flow appears to act as a backward facing step, leading to a persistent linear shadow zone where shear velocities approach 0 in the immediate lee of the lobe and gradually increase downwind as the flow recovers (Figures 1b and 2b).

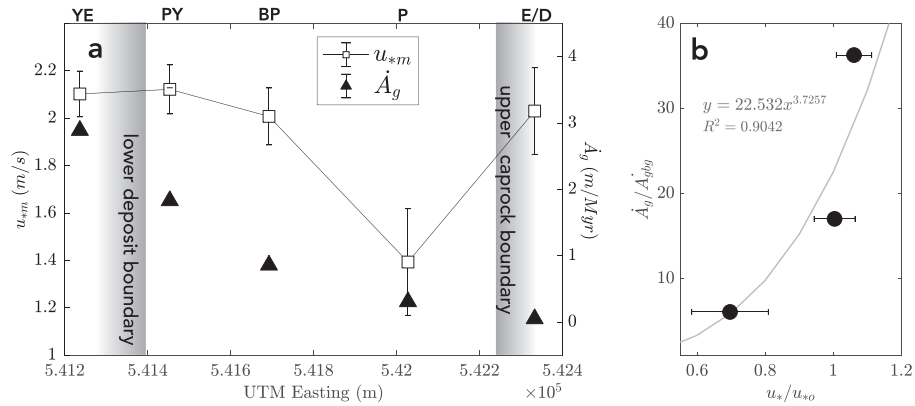


**Figure 3.** Average modeled shear velocities and measured wind abrasion rates along an east-west cross section of the Carcote ignimbrite. (a) Plot showing latitudinal profiles of modeled wind shear velocity ($u_*$, white squares) and calculated geologic abrasion rates ($\dot{A}_g$, black triangles) across the Carcote ignimbrite. Error estimates for the lava flow age are ±0.15 Ma, and $\dot{A}_g$ error bars fall within the symbol. Error estimates for modeled shear velocity values reflect the standard deviation of $u_*$ within each mapped polygon. Letters above plot correspond to mapped morphologic regimes described in Figure 2. Gray gradients mark locations where the upper caprock has not yet been breached at the boundary of $E/D$, leading to a reduction in abrasion susceptibility $S_a$ (right), and where the entire ignimbrite deposit has been breached, leading to an increase in $S_a$ (left). (b) Plot of relative abrasion rate as a function of modeled shear velocity for regions *PY*, *BP*, and *P*.

Comparison of $u_*$ and $\dot{A}_g$ values across the Carcote reveals that changes in $\dot{A}_g$ cannot be explained by variations in wind shear velocity alone, and observations from imagery show that significant lithologic boundaries are crossed at the windward escarpment along regions *YE* and $E/D$ (Figures 3a and S3). Therefore, we hypothesize that variations in the abrasion susceptibility of the the escarpment base exerts a first-order control on $\dot{A}_g$. This is because a weak base can be preferentially abraded, leading to undermining and block toppling of the upper resistant unit (de Silva et al., 2010; Perkins et al., 2015).

Eolian abrasion rate has been shown to be proportional to the kinetic energy flux of windblown particles, such that

$$\dot{A} = S_a q_{ke} \tag{1}$$

where $q_{ke}$ represents the instantaneous horizontal kinetic energy flux of particles to a unit area wind-perpendicular surface, and $S_a$ represents the susceptibility of a material to abrasion (Anderson, 1986, his equation 2a).

Wind tunnel experiments by Greeley et al. (1982) show that $S_a$ itself is proportional to the particle mass and the square of the particle velocity, that is, the particle kinetic energy, and that $S_a$ for volcanic tuffs can vary by an order of magnitude depending on their degree of welding.

Because the resistant upper caprock has not been breached along $E/D$ (Figure S3), the block toppling process has not been initiated and therefore low $\dot{A}_g$ rates persist. This is evidenced by more gently sloping channel walls upstream of the boundary (Figures S3a and 2c). In this case, even though modeled wind velocities are high, the apparent relative low $S_a$ value of the more resistant caprock leads to the lowest $\dot{A}_g$ rates in the study area.

Similarly, along *YE*, breaching of the ignimbrite's lower boundary along the channel and exposure of the underlying granular unit at the escarpment face appears to enhance windward erosion (Figures 2 and 3a). At these two sites, then, variations in $S_a$ appear to exert a dominant control on $\dot{A}_g$.

Along zones *PY*, *BP*, and *P*, channel relief and lithologic conditions appear largely similar, and we can explore the relationship between $\dot{A}_g$ and $q_{ke}$ caused by variable topographic shielding. $q_{ke}$ varies with the mass flux of sediment $Q$, which itself depends on shear velocity (Anderson, 1986). For the case of saltating particles, most classic relations show that $Q \propto u_*^3$ (Kok et al., 2012, their Table 2.1), and therefore $\dot{A} \propto u_*^5$. However, as Kok et al. (2012) note, this relationship depends on the assumption that particle speeds in saltation scale linearly with $u_*$. A recent comprehensive field study by Martin and Kok (2017) shows that saltating particle velocities are essentially constant, implying that $Q \propto u_*^2$ (i.e., saltating sediment mass flux is linearly

proportional to surface shear stress $\tau_b$) and therefore that abrasion rate should scale with shear velocity to the fourth power.

In Figure 3b, we plot the mean shear velocities relative to the incident shear velocity $u_{*o}$ for *PY*, *BP*, and *P* as a function of their measured increase in abrasion rates above the background value measured at $E/D$. From a power-law fit to the data, we find that increases in $\dot{A}_g/\dot{A}_{gbg}$ scale with $u_*/u_{*o}$ to the $\sim$ 3.7 power. This scaling is more consistent with $\dot{A} \propto u_*^4$ and therefore with a saltation mass flux relationship where particle velocities are generally constant within the saltation cloud (Martin & Kok, 2017). This claim should be approached with caution, though, as it is tenuous at best to infer particle trajectory characteristics from erosion rates calculated over million-year timescales, particularly with sparse data.

Throughout our study area, escarpment relief is ultimately controlled by the fluvial bedrock channel, which still appears to be transiently incising headward into the ignimbrite given the presence of a knickpoint and accompanying change in channel slope and relief upstream of the study regions (Figure S3c). This poses an additional difficulty in interpreting our $\dot{A}_g$ measurements because the windward escarpment relief, set by the incision history of the bedrock channel, is a time-transgressive boundary.

We can assess the effect an upstream-unzipping escarpment on our calculated erosion rates by estimating the vertical bedrock channel incision rate due to passage of an upstream-propagating knickpoint. Using a common knickpoint celerity model (e.g., Berlin & Anderson, 2007; Rosenbloom & Anderson, 1994), vertical incision rate $\mathrm{d}z/\mathrm{d}t$ is equal to the product of knickpoint slope $\mathrm{d}z/\mathrm{d}x$ and the knickpoint celerity $\mathrm{d}x/\mathrm{d}t$. Assuming a stream power model for fluvial bedrock incision, $\mathrm{d}x/\mathrm{d}t$ should scale with the upstream drainage area $A$ and the detachment-limited erosion coefficient $K$ (Berlin & Anderson, 2007). For our purposes, however, we use an average celerity of $\sim$ 680 m/Myr derived from the horizontal knickpoint retreat distance divided by the lava flow age (Figure S3). We also use the channel longitudinal profile to calculate a knickpoint slope of $\sim$ 0.05. This gives us a vertical incision rate of $\sim$ 37 m/Myr. For a mean channel relief 7.7±2.9 m (mean ± standard deviation, $n = 569$) downstream of the knickpoint, the vertical incision timescale is $\sim$ 0.2 Myr, much less than the total time of escarpment exposure to abrasion. We can therefore neglect the influence of the bedrock incision history in controlling the observed variability in $\dot{A}_g$.

### 4.2. Abrasion Patterns

The variability in modeled $u_*$ is accompanied by changes in erosional morphology across the ignimbrite, suggesting a relationship between flow strength, ignimbrite structure, and landscape form. We hypothesize that when wind speeds are sufficiently slow, such as in the wake of the lava lobe, sediment flux is dominated by bedload transport and particles are deflected along fracture paths that then become erosional troughs. Conversely, with higher shear velocities, larger particles that are less sensitive to topographic steering can be lifted in suspension, abrade higher relief topography, and impact downwind bedrock blocks directly.

These competing processes can be represented by the relationship between two nondimensional numbers, the Rouse number $P$ and the Stokes number $Stk$. The Rouse number reflects a flow's ability to suspend sediment and is the ratio between the particle settling velocity and the fluid shear velocity:

$$P = \frac{W_s}{u_* \kappa} \tag{2}$$

$P$ values greater than $\sim$ 2.5 ($W_s \approx u_*$) indicate predominantly bedload transport, and at $P < 1.2$ sediment is travelling fully in suspension. The Stokes number $Stk$ (also referred to by Anderson, 1986 as the inertial parameter $K$, after Langmuir & Blodgett, 1946) compares the response time of a particle to flow velocity changes to the intrinsic timescale set by the obstacle geometry (Anderson, 1986). It is defined as

$$Stk = \frac{\rho_p D^2 U}{18 \rho_a \nu a} \tag{3}$$

where $\nu$ is the kinematic viscosity of air and $a$ is the obstacle scale. When $Stk \ll 1$, particles should accurately trace streamlines and thus avoid impacting the obstacle. When $Stk \approx 1$, the obstacle timescale is equal to the particle relaxation time, and in this case a particle will tend to impact the downwind surface if there is significant flow curvature (Wessel & Righi, 1988). When $Stk \gg 1$, the initial particle launch trajectories should be largely decoupled from streamline curvature around the obstacle due to the particle's inertia. This leads to a high collection efficiency, which is the ratio of particles impacting an obstacle that pass through its projected area (e.g., Anderson, 1986; Wessel & Righi, 1988).

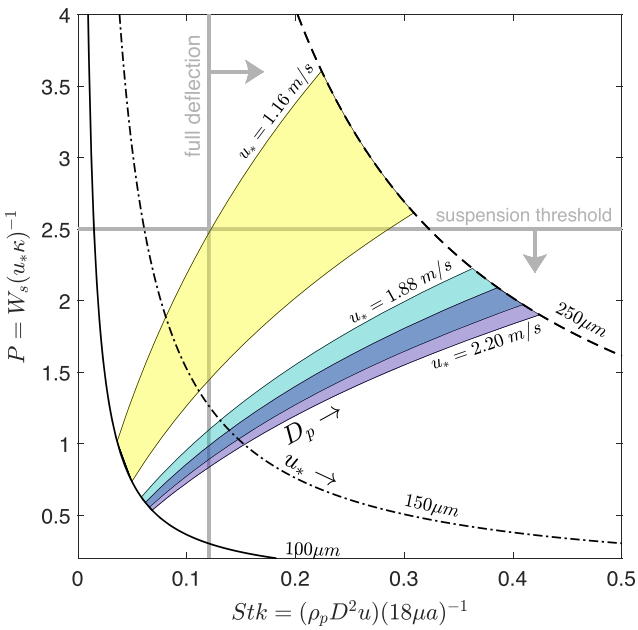


**Figure 4.** Comparison of modeled Rouse numbers (*P*, *y* axis) and Stokes numbers (*Stk*, *x* axis) for subregions *PY* (dark blue), *BP* (lighter blue), and *P* (yellow) within the Carcote ignimbrite. Horizontal arrow points towards increasing collection efficiency, and vertical arrow points toward increasing suspension. Inertial parameters are calculated at 1 m elevations for an average polygon diameter of 30 m. Colored sectors correspond to $u_*$ ranges at each site, and grain size contours for 100, 150, and 250 μm are shown through the parameter space.

In Figure 4, we plot the range of modeled shear velocities for our subregions within the framework of their respective Rouse and Stokes numbers for 100–250 μm particle sizes. Toward the low-velocity lava flow wake, modeled Rouse numbers decrease as Stokes numbers increase. At the most protected site *P* (yellow), a higher proportion of the particles would be fully deflected around ∼ 30 m radius bedrock polygon, and the coarsest sand fraction would be below the suspension threshold. Therefore, topographic steering should exert a much stronger control on particle transport pathways, and collection efficiency should be limited.

At site *BP* where polygons become bisected by wind-parallel erosional troughs, $u_* \approx 1.9$ m/s. The 250 μm sand should be in the suspension regime, and small increases in $u_*$ begin to yield large increases in *Stk* and hence decreases in topographic particle steering. Furthermore, once a wind-parallel channel is established, it can lead to a positive feedback by (1) creating a depression to focus sediment, and (2) effectively decreasing the obstacle radius by half and therefore doubling *Stk* and increasing collection efficiency.

Although we only show model results for an incident shear velocity of 2.0 m/s, this value likely reflects the strongest winds that the landscape experiences, and therefore the pattern of these results that is set by topography should only be enhanced with slower wind events. In other words, the shielded sector of the Carcote will only be more likely to have particles deflected around bedrock polygons in slower wind events.

Together these results suggest that the phase space defined by the Rouse and Stokes numbers provides a useful construct for interpreting the erosional patterns formed in planetary bedrock landscapes. For example, if bedrock fracture spacing leads to larger obstacle diameters than can be overcome by the regional wind strength and particle inertia, polygonal terrain should dominate. This could help explain mechanistically the colocation of yardangs and polygonal mesas on Mars in places like Mangala Valles (e.g., Figure S1) where local weather data is more difficult to obtain, in addition to the widespread occurrence of polygonal terrain on the Martian surface more generally (e.g., Irwin et al., 2004; Sharp, 1973).

In this study, we demonstrate that large-scale aerodynamic variation set by regional structures can modulate long-term wind abrasion morphology and landscape evolution rates, which vary by over 2 orders of magnitude within our study area in Northern Chile. We also show that the presence or absence of relatively weak units at the escarpment base can exert a first-order control on long-term eolian erosion rates.

Further, fracture-controlled (polygon) and flow-controlled (yardang) bedrock windscapes reflect a competition between downwind obstacle geometry, flow strength, and particle size classes available for abrasion. A phase space between Rouse and Stokes numbers can help delineate morphologic regimes.

Lastly, preferential erosion along cooling joints within volcanic deposits on Earth can yield polygonal terrain similar to fretted terrain on Mars and may therefore provide a simple null hypothesis against which to test more dynamic models (e.g., landslides, slumps) responsible for their occurrence (e.g., Irwin et al., 2004).

**Acknowledgments**
Additional explanation, figures, and weather station data can be found in our supporting information. Reviews by Doug Jerolmack, David Rubin, and one anonymous reviewer, in addition to constructive discussion with Mikael Witte, greatly enhanced the quality of this manuscript.Funding for J. P. P. was provided by the USGS Geology, Minerals, Energy, and Geophysics Science Center. S. de S. acknowledges funding from NASA Grant 16-SSW16_2-0141 to conduct Mars analog studies in the Altiplano-Puna.

## References

Anderson, R. S. (1986). Erosion profiles due to particles entrained by wind: Application of an eolian sediment- transport model. *Geological Society of America Bulletin*, *97*, 1270–1278. https://doi.org/10.1130/0016-7606(1986)97<1270:EPDTPE>2.0.CO;2

Bailey, J. E., Self, S., Wooller, L. K., & Mouginis-Mark, P. J. (2007). Discrimination of fluvial and eolian features on large ignimbrite sheets around La Pacana Caldera, Chile, using Landsat and SRTM-derived DEM. *Remote Sensing of Environment*, *108*, 24–41. https://doi.org/10.1016/j.rse.2006.10.018

Baker, M. C. W., & Francis, P. W. (1978). Upper Cenozoic volcanism in the Central Andes—Ages and volumes. *Earth and Planetary Science Letters*, *41*, 175–187. https://doi.org/10.1016/0012-821X(78)90008-0

Berlin, M. M., & Anderson, R. S. (2007). Modeling of knickpoint retreat on the Roan Plateau, western Colorado. *Journal of Geophysical Research*, *112*, F03S06. https://doi.org/10.1029/2006JF000553

Bridges, N. T., & Laity, J. E. (2013). Fundamentals of Aeolian sediment transport: Aeolian abrasion. In J. Shroder (Editor in Chief), N. Lancaster, D. J. Sherman, & A. C. W. Baas (Eds.), *Treatise on geomorphology*, Aeolian Geomorphology (Vol. 11, pp. 134148). San Diego CA: Academic Press

Burkow, M., & Griebel, M. (2016). A full three dimensional numerical simulation of the sediment transport and the scouring at a rectangular obstacle. *Computers and Fluids*, *125*, 1–10. https://doi.org/10.1016/j.compfluid.2015.10.014

Cook, K. L., Turowski, J. M., & Hovius, N. (2013). A demonstration of the importance of bedload transport for fluvial bedrock erosion and knickpoint propagation. *Earth Surface Processes and Landforms*, *38*, 683–695. https://doi.org/10.1002/esp.3313

de Silva, S. L., Bailey, J. E., Mandt, K. E., & Viramonte, J. M. (2010). Yardangs in terrestrial ignimbrites: Synergistic remote and field observations on Earth with applications to Mars. *Planetary and Space Science*, *58*, 459–471. https://doi.org/10.1016/j.pss.2009.10.002

de Silva, S. L., & Francis, P. (1991). *Volcanoes of the Central Andes*. Berlin; New York: Springer-Verlag.

de Silva, S. L., Spagnuolo, M. G., Bridges, N. T., & Zimbelman, J. R. (2013). Gravel-mantled megaripples of the Argentinean Puna: A model for their origin and growth with implications for Mars. *Bulletin of the Geological Society of America*, *125*, 1912–1929. https://doi.org/10.1130/B30916.1

Garreaud, R., Vuille, M., & Clement, A. C. (2003). The climate of the Altiplano: Observed current conditions and mechanisms of past changes. *Palaeogeography, Palaeoclimatology, Palaeoecology*, *194*, 5–22.

Greeley, R., & Iversen, J. D. (1985). Wind as a geological process on Earth, Mars, Venus and Titan. *Wind as a geological process on Earth, Mars, Venus and Titan* (p 333). New York: Cambridge University Press.

Greeley, R., Iversen, J. D., Pollack, J. B., Udovich, N., & White, B. (1974). Wind tunnel simulations of light and dark streaks on Mars. *Science*, *183*, 847–849. https://doi.org/10.1126/science.183.4127.847

Greeley, R., Leach, R. N., Williams, S. H., White, B. R., Pollack, J. B., Krinsley, D. H., & Marshall, J. R. (1982). Rate of wind abrasion on Mars. *Journal of Geophysical Research*, *87*, 10,009–10,024. https://doi.org/10.1029/JB087iB12p10009

Hugenholtz, C. H., Barchyn, T. E., & Favaro, E. A. (2015). Formation of periodic bedrock ridges on Earth. *Aeolian Research*, *18*, 135–144. https://doi.org/10.1016/j.aeolia.2015.07.002

Irwin, R. P., Watters, T. R., Howard, A. D., & Zimbelman, J. R. (2004). Sedimentary resurfacing and fretted terrain development along the crustal dichotomy boundary, Aeolis Mensae, Mars. *Journal of Geophysical Research*, *109*, E09011. https://doi.org/10.1029/2004JE002248

Kok, J. F., Parteli, E. J. R., Michaels, T. I., & Karam, D. B. (2012). The physics of wind-blown sand and dust. *Reports on Progress in Physics*, *75*, 106901. https://doi.org/10.1088/00344885/75/10/106901

Langmuir, I., & Blodgett, K. (1946). *A mathematical investigation of water droplet trajectories*. Washington, DC: Army Air Forces Headquarters, Air Technical Service Command; distributed by Office of the Publication Board, Dept. of Commerce. Retrieved from file://catalog.hathitrust.org/Record/101738423 http://hdl.handle.net/2027/uiug.30112040709120

Mandt, K. E., de Silva, S. L., Zimbelman, J. R., & Crown, D. A. (2008). Origin of the Medusae Fossae Formation, Mars: Insights from a synoptic approach. *Journal of Geophysical Research*, *113*, E12011. https://doi.org/10.1029/2008JE003076

Martin, R. L., & Kok, J. F. (2017). Wind-invariant saltation heights imply linear scaling of aeolian saltation flux with shear stress. *Science Advances*, *3*, e1602569. https://doi.org/10.1126/sciadv.1602569

Ojha, L., & Lewis, K. (2018). The density of the Medusae Fossae Formation: Implications for its composition, origin, and importance in Martian history. *Journal of Geophysical Research: Planets*, *123*, 1368–1379. https://doi.org/10.1029/2018JE005565

Pelletier, J. D. (2018). Controls on yardang development and morphology: 2. Numerical modeling. *Journal of Geophysical Research: Earth Surface*, *123*, 723–743. https://doi.org/10.1002/2017JF004462

Pelletier, J. D., Kapp, P. A., Abell, J., Field, J. P., Williams, Z. C., & Dorsey, R. J. (2018). Controls on yardang development and morphology: 1. Field observations and measurements at Ocotillo Wells, California. *Journal of Geophysical Research: Earth Surface*, *123*, 694–722. https://doi.org/10.1002/2017JF004461

Perkins, J. P., Finnegan, N. J., & De Silva, S. L. (2015). Amplification of bedrock canyon incision by wind. *Nature Geoscience*, *8*, 305. https://doi.org/10.1038/ngeo2381

Rosenbloom, N. A., & Anderson, R. S. (1994). Hillslope and channel evolution in a marine terraced landscape, Santa Cruz, California. *Journal of Geophysical Research*, *99*, 14,013–14,029.

Sharp, R. P. (1973). Mars: Fretted and chaotic terrains. *Journal of Geophysical Research*, *78*, 4073–4083. https://doi.org/10.1029/JB078i020p04073

Strecker, M. R., Alonso, R. N., Bookhagen, B., Carrapa, B., Hilley, G. E., Sobel, E. R., & Trauth, M. H. (2007). Tectonics and climate of the southern Central Andes. *Annual Review of Earth and Planetary Sciences*, *35*, 747–787. https://doi.org/10.1146/annurev.earth.35.031306.140158

Vuille, M. (1999). Atmospheric circulation over the Bolivian Altiplano during dry and wet periods and extreme phases of the southern oscillation. *International Journal of Climatology*, *19*, 1579–1600. https://doi.org/10.1002/(SICI)1097-0088(19991130)19:14<1579::AID-JOC441>3.0.CO;2-N

Wang, Z. T., Wang, H. T., Niu, Q. H., Dong, Z. B., & Wang, T. (2011). Abrasion of yardangs. *Physical Review E - Statistical, Nonlinear, and Soft Matter Physics*, *84*, 031304. https://doi.org/10.1103/PhysRevE.84.031304

Ward, A. W., & Greeley, R. (1984). Evolution of the yardangs at Rogers Lake, California. *Geological Society of America Bulletin*, *95*, 829–837. https://doi.org/10.1130/0016-7606(1984)95<829:EOTYAR>2.0.CO;2

Wessel, R. A., & Righi, J. (1988). Generalized correlations for inertial impaction of particles on a circular cylinder. *Aerosol Science and Technology*, *9*, 29–60. https://doi.org/10.1080/02786828808959193

Worner, G., Hammerschmidt, K., Henjes-Kunst, F., Lezaun, J., & Wilke, H. (2000). Geochronology (Ar-40/Ar-39, K-Ar and He-exposure ages) of Cenozoic magmatic rocks from Northern Chile (18–22°S): Implications for magmatism and tectonic evolution of the central Andes. *Revista Geologica De Chile*, *27*, 205–240.